JOURNAL OF GEOPHYSICAL RESEARCH, VOL. 113, B12411, doi:10.1029/2008JB005724, 2008

Coseismic strengthening of the shallow portion of the subduction fault and its effects on wedge taper

Yan Hu[1] and Kelin Wang[1,2]

Received 28 March 2008; revised 17 September 2008; accepted 14 October 2008; published 23 December 2008.

[1] According to the dynamic Coulomb wedge model, coseismic strengthening of the shallowest part of the subduction interface can cause permanent deformation of the overlying outer wedge, so that the cumulative effects of great interplate earthquakes control the geometry of the wedge. In this work, we use a numerical model, which is a hybrid of the frictional contact model and the classical crack model, to study how stress is coseismically transferred from the seismogenic zone to the strengthening updip zone to cause wedge deformation. In this static model, the ''critical strengthening'' required to prevent the rupture from breaking the trench depends on the force drop of the seismogenic zone, defined as the product of the average shear stress drop and the area of the seismogenic zone. In a simple model of uniform material properties with a few megapascals average stress drop over a seismogenic zone of 120 km downdip width, the critical strengthening for a 30 km wide updip zone is an increase in the effective friction coefficient by about 0.05. Using the Coulomb wedge theory, we demonstrate that this level of strengthening can readily push the overlying wedge into a critical state of failure. With much greater strengthening, the rupture is able to extend into the updip zone only slightly, causing localized wedge compression in the area of slip termination. We examined wedge geometry of 22 subduction zones in the light of the model results. We found that the surface slope of these wedges is generally too high to be explained using the classical wedge theory but can be explained using the dynamic Coulomb wedge model including coseismic strengthening of the shallow portion of the megathrust.

Citation: Hu, Y., and K. Wang (2008), Coseismic strengthening of the shallow portion of the subduction fault and its effects on wedge taper, *J. Geophys. Res.*, *113*, B12411, doi:10.1029/2008JB005724.

1. Introduction

[2] Deformation, stress, and geometry of the wedge-shaped geological unit at the leading edge of the upper plate of subduction zones are of interest because they provide information on the frictional properties of the subduction fault. Most studies investigating the mechanics of the wedge only address the long-term state of stress averaged over numerous earthquake cycles, and the wedge is assumed to be always on the verge of Coulomb failure. Recently, *Wang and Hu* [2006] proposed the dynamic Coulomb wedge theory to address the effects of stress changes along the subduction fault in great earthquakes.

[3] The frictional strength of the seismogenic zone of the subduction fault decreases during an earthquake, causing a stress drop (Figure 1). In contrast, the strength of the shallowest part of the subduction interface extending to several to ~10 km depths increases during an earthquake, resisting rupture (Figure 1). Direct and indirect evidence for this coseismic strengthening behavior has been summarized by *Wang and He* [2008]. The most direct evidence comes from near-trench continuous monitoring of coseismic deformation of the M 8.2 Tokachi-oki earthquake of 2003 [*Baba et al.*, 2006] and the M 8.7 Nias-Simeulue earthquake of 2005 [*Briggs et al.*, 2006; *Hsu et al.*, 2006]. The segment of the fault downdip of the seismogenic zone also strengthens during an earthquake, and materials at even great depths undergo viscous deformation. The updip and downdip limits of the seismogenic zone are thought to be thermally and petrologically controlled [e.g., *Hyndman and Wang*, 1993; *Hyndman et al.*, 1997].

[4] Subduction zones can be roughly grouped into the accretionary and erosional types [*von Huene and Scholl*, 1991; *Clift and Vannucchi*, 2004], depending on whether there is net accretion of material or continuing removal of material from the underside of the upper plate, respectively, in the recent geological past. Regardless of the difference between accretion and erosion, the frontal part of the overlying plate, referred to as the outer wedge, features active ongoing permanent deformation, while the part further landward, referred to as the inner wedge, usually shows much less recent permanent deformation [*von Huene and Klaeschen*, 1999; *Park et al.*, 2002; *Krabbenhöft et al.*, 2004] (Figures 1b and 1c). In addition, the surface slope of the outer wedge is generally steeper than that of the inner

[1]School of Earth and Ocean Sciences, University of Victoria, Victoria, British Columbia, Canada.
[2]Pacific Geoscience Centre, Geological Survey of Canada, Sidney, British Columbia, Canada.

0148-0227/08/2008JB005724$09.00

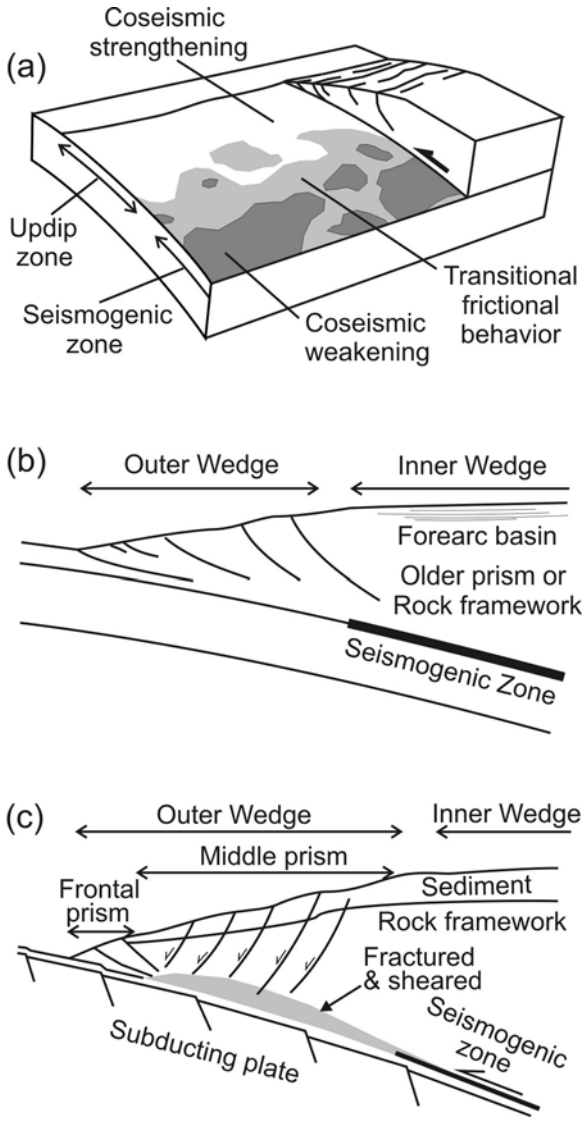

Figure 1. (a) Cartoon showing spatial variations in the frictional properties of a subduction fault, based on a similar figure by *Wang and Hu* [2006]. (b) A 2-D simplification of the system shown in Figure 1a for accretionary margins (based on *Wang and Hu* [2006]). (c) A 2-D simplification for erosional margins based on concepts presented by *von Huene et al.* [2004].

wedge. *Wang and Hu* [2006] postulate that the structural and morphological contrasts are associated with the frictional property change along the subduction fault: The outer wedge overlies the aseismic updip zone, and the inner wedge overlies the seismogenic zone (Figures 1b and 1c); it is the coseismic strengthening of the shallow aseismic zone that repeatedly drives the outer wedge into a failure state and controls its long-term geometry.

[5] However, coseismic stress increase in the updip zone cannot be arbitrarily large; it is related to the size of the earthquake. Questions to be addressed include how the coseismic stress changes in different parts of the subduction fault are "coordinated" in an earthquake, what part of the shallow segment experiences strengthening during an earthquake, how much driving force an earthquake can provide to deform a wedge of given strength, and what parameters of the earthquake control the driving force. In this work, we first develop an elastic two-dimensional (2-D) finite element model to investigate how stress is transferred from the seismogenic zone to the shallow segment during an earthquake. To apply the model results to real subduction zones, we compile outer wedge geometry for many subduction zones. Finally, with the knowledge of coseismic stress transfer and the observed wedge geometry, we discuss the mechanics of the outer wedges as affected by great earthquakes.

2. Coseismic Strength Change Along the Subduction Fault

2.1. Model of Stress Transfer

[6] We describe stress changes along the subduction fault during a great earthquake using a three-segment model including a seismogenic zone between updip and downdip strengthening segments (Figure 2). In this static model, a prescribed sudden decrease in frictional strength causes the seismogenic zone to slip, but a prescribed strength increase causes the segments updip and downdip to resist slip. Therefore, the shear stress over the seismogenic zone is coseismically transferred to the other two segments. This model builds upon classical static earthquake models such as the dislocation model in which slip distribution is prescribed and the crack models in which the stress distribution is prescribed (Appendix A), but it incorporates contrasting frictional behaviors of different parts of the fault. For simplicity and for the convenience of directly applying the model results to wedge mechanics in later sections, we assume a constant $\Delta\mu_b'$ for each fault segment. This simple trisegment parameterization captures the most fundamental aspect of earthquake rupture, that is, the simultaneous weakening of the seismogenic zone and

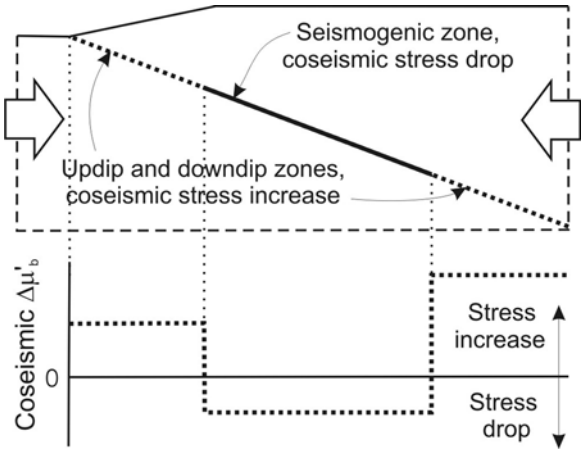

Figure 2. Schematic illustration of the subduction zone model considered in this work. Large arrows represent interseismic strain accumulation. An earthquake is simulated by imposing a sudden decrease in the effective friction coefficient μ_b' of the seismogenic zone by the amount of $\Delta\mu_b'$. Coseismic strengthening of the updip and downdip zones is simulated by imposing a sudden increase in their μ_b' values.

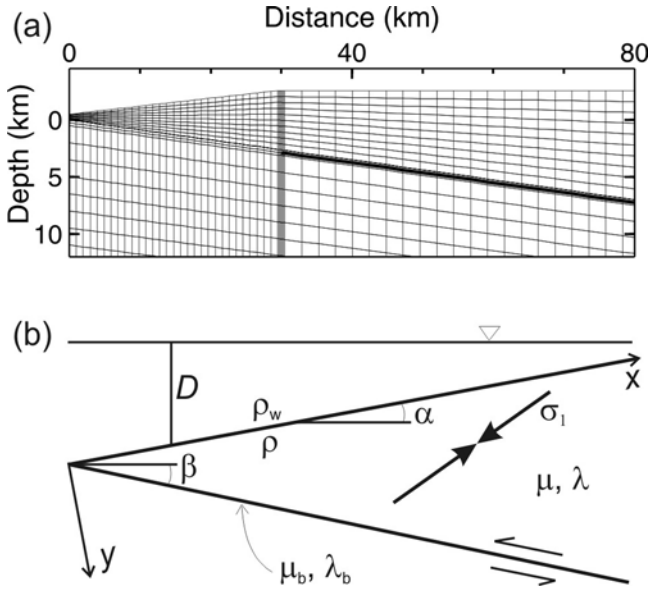

Figure 3. (a) Central part of the finite element mesh for the stress transfer model discussed in section 2. Thick solid line along the megathrust fault ($\geq$30 km distance) marks the location of the seismogenic zone. (b) Illustration of the Coulomb wedge model for the most frontal part of the upper plate to be discussed in section 3, showing the coordinate system (x, y), example maximum compressive stress σ_1, angles α and β, and water depth D. Here ρ and ρ_w are densities of the wedge material and overlying water, respectively. Here μ_b and λ_b are friction coefficient and pore fluid pressure ratio along the basal fault, respectively, and μ and λ are internal friction coefficient and internal pore fluid pressure ratio, respectively.

strengthening of its neighboring areas of the fault, yet still retains the simplicity of the classical models to allow clear explication of physical concepts.

[7] The real subduction fault zone has a finite thickness, and the evolution of stresses along the fault during an earthquake must be dynamic and nonlinear. If we assume that the laboratory-derived rate- and state-dependent friction law [*Ruina*, 1983; *Marone et al.*, 1991; *Dieterich*, 1992] applies to real faults, the observed coseismic strengthening and weakening of the faults can be parameterized in terms of positive and negative, respectively, logarithmic dependence of their friction coefficients on slip rate. For the purpose of the present study, we only need to consider the net change in the shear stress along the fault, and we do not model the time-dependent evolution of fault friction. It is this net change that controls the overall coseismic deformation of the overlying outer and inner wedges.

[8] In this section, we use a 2-D plane strain finite element model of elastic material to model the net stress change along the fault during an earthquake (Figure 3a). In section 3, we will study the consequence of this stress change to the mechanics of the outer wedge, and the fault stress studied here will be used as a boundary condition at the base of the wedge (Figure 3b). The strategy of separately studying the stress transfer along the fault and the mechanics of the wedge greatly simplifies the problem. A disadvantage of this separation is that the elastic stress transfer model does not account for any permanent coseismic deformation of the outer wedge and its potential nonlinear effect on fault stress. However, permanent wedge deformation during an individual earthquake is very small, and this second-order effect should introduce little error to the stress transfer modeling. Another simplification is to consider internal pore fluid pressure only in the Coulomb wedge model but ignore it in the stress transfer model. The pore fluid pressure can modify the elastic deformation in the stress transfer model only slightly, but its effect on the yield strength of a Coulomb wedge is of first-order and cannot be ignored. Similarly, pore fluid pressure along the fault zone has a first-order impact on fault strength and cannot be ignored. Its effect is included in the effective coefficient of friction μ_b' of the fault, which is the ratio of the shear strength and normal stress and is a composite parameter.

[9] Except for a planar fault, which is sufficient for the purpose of the present work, our model setup follows that of *Wang and He* [2008]. The method of Lagrange multiplier Domain Decomposition [*Wang and He*, 1999] is used to handle the frictional contact between the two converging plates. The model boundaries are set to be very far away from the area of interest, the updip zone and seismogenic zone of the megathrust, in order to minimize potential artifacts of these boundaries. The resultant very large vertical dimension of the model domain would lead to very large lithostatic pressures at large depths and cause numerical problems to the calculation of shear stresses if gravity were directly included. Therefore, we invoke gravity (assuming a rock density of 2800 kg/m^3) only when determining yield stresses along the fault and exclude it from deformation calculation.

[10] Modeling of the stress transfer includes two steps, fault locking (interseismic) followed by an earthquake (coseismic). The interseismic stress buildup is modeled by moving the remote seaward and landward model boundaries toward each other against a locked fault that is on the verge of frictional failure (Figure 2). On the basis of the weak fault arguments as summarized by *Wang and Hu* [2006], we use $\mu_b' = 0.04$ for the updip and seismogenic zones. The stress in the deeper segment is expected to be much relaxed a long time after the earthquake, and we use $\mu_b' = 0.004$ to represent its nearly zero strength.

[11] The earthquake is simulated by imposing a sudden decrease in the effective friction coefficient of the seismogenic zone, that is, a negative $\Delta\mu_b'$ (Figure 2). The elastic strain accumulated in the system at the interseismic step will then cause the fault to slip. Coseismic stress drops as constrained by seismological studies vary with the types and magnitudes of earthquakes from a few kilopascals to a few tens of megapascals [e.g., *Kanamori*, 1994]. In this work, $\Delta\mu_b'$ along the seismogenic zone is chosen to produce a stress drop of a few megapascals, typical of great subduction earthquakes. The corresponding strengthening of the updip and downdip segments is simulated by imposing a positive $\Delta\mu_b'$ (Figure 2). We apply different values of $\Delta\mu_b'$ to the shallow segment updip of the seismogenic zone to represent different degrees of coseismic strengthening. The exact degree of strengthening of the aseismic segment downdip of the seismogenic zone is less important for the purpose of our study and, for the sake of simplifying the

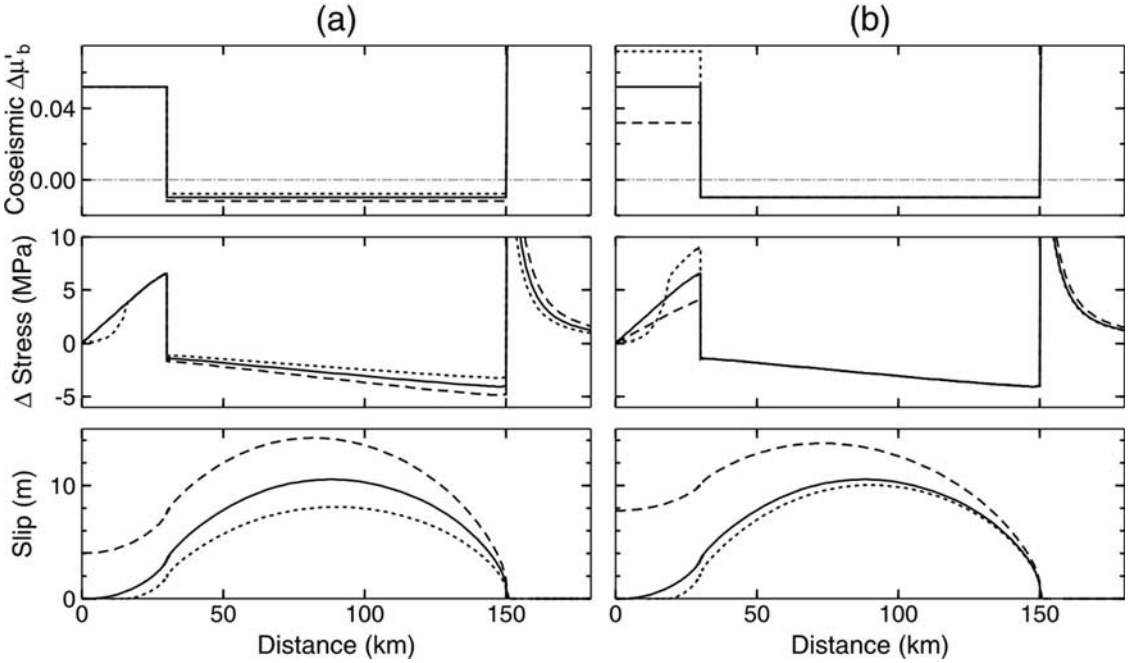

Figure 4. Examples to illustrate the effects of earthquake size and the degree of the coseismic strengthening of the updip zone. (a) Identical strengthening of the updip zone but different stress drops in the seismogenic zone. (b) Identical stress drop in the seismogenic zone but different degrees of strengthening of the updip zone. Figures 4a (top) and 4b (top) show coseismic strength change $\Delta\mu_b'$ along the fault. Figures 4a (middle) and 4b (middle) show stress change. Figures 4a (bottom) and 4b (bottom) show slip distribution. Solid lines represent the reference earthquake model. The central part of the finite element mesh for these models is shown in Figure 3a.

physical problem, we use a sufficiently large $\Delta\mu_b'$ to prevent it from having any coseismic slip.

2.2. Reference Earthquake Model

[12] For a reference earthquake model, we use horizontal widths of 30 km and 120 km for the updip zone and the seismogenic zone, respectively. On the basis of observed average geometry of subduction zone fore arcs (to be explained in section 3.2), we assume surface slope angles $\alpha = 4°$ and $0°$ for the outer wedge and areas further landward, respectively, and a constant basal dip $\beta = 5°$ for the subduction fault. Following *Wang and He* [2008], we use a moderate rigidity of 40 GPa and a Poisson's ratio of 0.25. It can be shown that changing the rigidity value only causes a scaling change to the amount of fault slip and has no effects on the stresses. Our numerical experiments have shown that the effect of reasonable variation of rigidity with depth on the stress solutions is nearly negligible (results not displayed). The effects of other model parameters will be tested by varying parameter values based on the reference earthquake model. The central part of the finite element mesh for the reference earthquake model is shown in Figure 3a, and the results are shown in both Figures 4a and 4b using solid lines.

[13] For the reference earthquake, $\Delta\mu_b' = -0.01$ is applied to the seismogenic zone, leading to an average stress drop of 2.8 MPa (solid lines in Figure 4). A strengthening of the updip zone by $\Delta\mu_b' = 0.052$ causes the coseismic slip to taper to zero at the trench (Figures 4a (bottom) and 4b (bottom), solid lines). If the model earthquake rupture is 500 km long in the strike direction, this reference earthquake would have a moment magnitude $M_w = 8.8$. The normal stress along the fault is determined mainly by the weight of the rock column above and shows little change during the earthquake, except in the vicinity of the transition between zones of strengthening and weakening. Because of the uniform $\Delta\mu_b'$ assumed for each fault segment, the shear stress increase or decrease with trench-normal distance follows a linear trend if the fault segment is everywhere at frictional failure. By using a heterogeneous $\Delta\mu_b'$, we could also produce a uniform stress drop along the seismogenic zone, simulating the classical crack model (see Appendix A). The abrupt stress change between the strengthening and weakening segments as shown in Figure 4 is the consequence of the abrupt change in $\Delta\mu_b'$ across segment boundaries. As will be discussed in section 4.2, a more gradual $\Delta\mu_b'$ change between segments will lead to a smoother stress change along the fault but will not change the basic characteristics of the results.

[14] The slip distribution along the fault in this model is similar to that of the classical crack model (Appendix A), but the updip termination of rupture is more gradual because the updip segment is allowed to slip in accordance with its coseismic frictional strength. This type of "bell-shaped" slip distribution is frequently seen in rupture models based on the inversion of geodetic and/or seismological observations, but heterogeneous frictional properties may give rise to other types of distribution [e.g., *Manighetti et al.*, 2005]. Although it is the stress change along the fault that is directly relevant to wedge deformation, it is important to

recognize that the slip distribution is critical to many other aspects of earthquake research such as the generation of tsunamis [*Geist and Dmowska*, 1999; *Wang and He*, 2008].

2.3. Coseismic Strengthening of the Updip Zone and Stress Drop in the Seismogenic Zone

[15] For the same degree of strengthening of the updip zone, different levels of stress drop in the seismogenic zone lead to different states of frictional failure in the updip zone. The three examples shown in Figure 4a have the same $\Delta\mu'_b$ value for the updip zone but different $\Delta\mu'_b$ values for the seismogenic zone. For the reference earthquake model (solid lines in Figure 4), the entire updip zone is at frictional failure. A larger earthquake occurring on the same seismogenic zone also pushes the entire updip zone to failure (dashed line), but the stress increase in the updip zone is the same as for the reference earthquake. The larger earthquake does not transfer more stress to the updip zone because the stress increase in the updip zone is limited by its $\Delta\mu'_b$. Instead, the "extra" stress due to the larger earthquake causes the entire updip zone to slip for a distance. A smaller earthquake only causes a deeper portion of the updip zone to fail (dotted line). In this case, the stress increase in this deeper portion is sufficient to resist the earthquake push, and it serves to create a stress "shadow" to protect the rest of the updip zone.

[16] Conversely, for the same stress drop in the seismogenic zone, different degrees of strengthening of the updip zone lead to different states of frictional failure of this zone. The three examples shown in Figure 4b have the same $\Delta\mu'_b$ value for the seismogenic zone but different $\Delta\mu'_b$ values for the updip zone. Given the stress drop shown in Figure 4b, the value of updip zone $\Delta\mu'_b = 0.052$ used for the reference earthquake model (solid lines) is the maximum strengthening with which the entire updip zone is at failure. Such a $\Delta\mu'_b$ value, denoted $\Delta\mu'_{b\_c}$, is called the critical strengthening in this work. If $\Delta\mu'_b$ is greater than $\Delta\mu'_{b\_c}$, such as 0.072, the strengthening is too large to allow the stress to be transferred to the entire updip zone, and the shallowest portion of the updip zone is in the stress shadow (dotted line). In this static model, the critical strengthening is also the minimum strengthening required to prevent the rupture from breaking the trench. If $\Delta\mu'_b$ is lower than $\Delta\mu'_{b\_c}$, such as 0.032, the resultant stress increase is too small to resist the push from the seismogenic zone, and the rupture breaks to the trench (dashed line). Similarly, the trench-breaking rupture of the dashed-line model in Figure 4a indicates that the $\Delta\mu'_b$ value of 0.052 assigned to the updip zone must be smaller than the critical strengthening for the larger earthquake. Although the slip distribution in these two trench-breaking rupture models (dashed lines in Figure 4) is similar to the results obtained by *Liu and Rice* [2007] using the rate- and state-dependant friction law for a model including a moderately rate-strengthening updip segment, it should be cautioned that a quantitative comparison cannot be made because our static model does not address any rate dependence of the fault strength.

[17] In general, for a state with $\Delta\mu'_b \le \Delta\mu'_{b\_c}$, the whole updip zone is at frictional failure. For a state with $\Delta\mu'_b > \Delta\mu'_{b\_c}$, its shallowest part is in a stress shadow. It needs to be pointed out that for states of $\Delta\mu'_b > \Delta\mu'_{b\_c}$, potential permanent deformation of the overlying outer wedge must be localized to the area around the termination of the coseismic slip where large shear stress increase takes place (e.g., the "spike" of the dotted line immediately updip of the seismogenic zone in Figure 4b). The exact Coulomb wedge solution [*Dahlen*, 1984; *Wang and Hu*, 2006] that we will use in later sections assumes a uniform wedge whose basal fault is either nowhere or everywhere at failure. To be able to combine the results of our finite element modeling with the Coulomb wedge solution, we focus only on the states of $\Delta\mu'_b \le \Delta\mu'_{b\_c}$. In the following sections, we mainly examine the state of $\Delta\mu'_b = \Delta\mu'_{b\_c}$, which is also representative of the states of $\Delta\mu'_b < \Delta\mu'_{b\_c}$. States of $\Delta\mu'_b > \Delta\mu'_{b\_c}$ may sometimes be applicable to real subduction zones and will be discussed in section 4.1.

2.4. Critical Strengthening of the Updip Zone and Force Drop in the Seismogenic Zone

[18] In this section, we investigate how the critical strengthening of the updip zone is related to the stress drop and the size of the seismogenic zone. In comparison with the reference earthquake model, we consider two models in which the seismogenic zone is either wider or narrower than the reference earthquake by 40 km (dashed and dotted lines in Figure 5). The seismogenic zone $\Delta\mu'_b$ values are chosen so that these two models and the reference model all have the same "force drop" ΔF, defined as the product of the average stress drop and area of the seismogenic zone. The ΔF for all the three models shown in Figure 5 is identically 3.3×10^{11} N per unit strike length. The model result show that all these models yield the same critical strengthening $\Delta\mu'_{b\_c} = 0.052$ for the updip zone (Figure 5a). Although these model earthquakes produce the same ΔF, their moment magnitudes are different, with the widest seismogenic zone (dotted lines) producing the largest M_w. It is the total push represented by ΔF, not M_w, that the updip zone "feels" from the seismogenic zone. $\Delta\mu'_{b\_c}$ is thus a function of ΔF only.

[19] Further model tests reveal a linear relationship between $\Delta\mu'_{b\_c}$ and ΔF (Figure 6). If all the force drop is balanced by the stress increase in the updip zone alone, ΔF should scale with $\Delta\mu'_{b\_c}$ times the square of the width of the updip zone (see equation (8) by *Wang and He* [1999]). But the scaling relation shown in Figure 6 is affected also by the stress increase downdip of the seismogenic zone. Figure 6 shows the simple fact that for a given width of the updip zone, an earthquake with a larger ΔF requires a greater $\Delta\mu'_{b\_c}$ to prevent the rupture from breaking the trench.

[20] With the horizontal width of the updip zone fixed, Figure 7 shows the effects of surface slope angle α and fault dip β on $\Delta\mu'_{b\_c}$. If α is larger, the fault is more deeply buried for the same horizontal distance from the trench. The greater normal stress makes the fault stronger, and therefore a smaller $\Delta\mu'_{b\_c}$ is sufficient to prevent trench-breaking rupture (Figure 7a). A larger β has a similar effect on $\Delta\mu'_{b\_c}$ (Figure 7b). Conversely, it is easier to drive the basal fault of a more narrowly tapered wedge to failure, and thus a greater $\Delta\mu'_{b\_c}$ is required to resist the earthquake push. Given the geometry of the system, a higher ΔF leads to a greater $\Delta\mu'_{b\_c}$, consistent with the results shown in Figure 6. For small-taper wedges with $\alpha + \beta < 10°$, $\Delta\mu'_{b\_c}$ is greatly affected by wedge geometry as well as the earthquake force

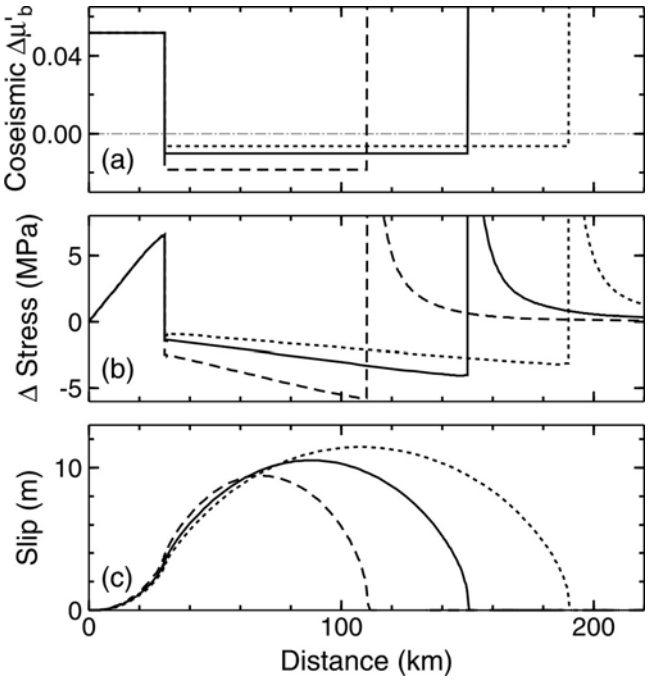

Figure 5. Three examples with different seismogenic zone widths but the same force drop $\Delta F = 3.3 \times 10^{11}$ N. (a) Coseismic $\Delta\mu'_b$ along the subduction fault. (b) Shear stress change along the fault. (c) Slip distribution. Results for the reference earthquake model shown in Figure 4 are reproduced here using solid lines. Models with seismogenic zone widths of 80 km and 160 km are represented by the dashed and dotted lines, respectively.

drop. For wedges with larger tapers, $\Delta\mu'_{b\_c}$ is less sensitive to further changes in wedge geometry.

3. Effects of the Coseismic Strengthening of the Updip Zone on Outer Wedge Geometry

3.1. Wedge Mechanics

[21] In section 2, we have described models that quantify stress transfer along the subduction fault during an earthquake. Here we briefly review the wedge mechanics theory to explain how stresses and stress changes along the fault control the stress field of the overlying wedge. We only summarize the simplest, exact analytical solution derived in the coordinate system shown in Figure 3b. If the wedge is in a yield state (critical wedge), it obeys the Coulomb failure criterion. If it is not in a yield state (stable wedge), it obeys Hooke's law of elasticity. For a wedge under water of density ρ_w and depth D (a function of x, see Figure 3b), a Hubbert-Rubey fluid pressure ratio λ within the wedge is defined as [*Dahlen*, 1984]

$$\lambda = \frac{P - \rho_w g D}{-\sigma_y - \rho_w g D} \tag{1}$$

where P is the internal pore fluid pressure, g is gravitational acceleration, σ_y is normal stress in the y direction.

[22] A similar definition of the pore fluid pressure ratio λ_b along the fault, proposed by *Wang et al.* [2006], allows us to establish a precise relationship between the shear stress τ along the fault and the effective normal stress $\bar{\sigma}_n (=\sigma_n + P)$ just above the fault. This relationship, stemming from the Coulomb friction criterion for the subduction fault, can be written as

$$\tau_n = -\frac{\mu_b(1-\lambda_b)}{1-\lambda}(\sigma_n + P) = -\mu'_b \frac{\bar{\sigma}_n}{1-\lambda} \tag{2}$$

where μ_b is the friction coefficient along the fault. If $\lambda_b \neq \lambda$, which implies that the hydrological process in the fault zone is very different from that in the wedge, the effective normal stresses within and just above the fault are different. With a constant λ_b, the effective friction coefficient is explicitly defined here as $\mu'_b = \mu_b\,(1 - \lambda_b)$. Note that in papers by *Dahlen* [1984], *Wang and Hu* [2006], and *Wang et al.*

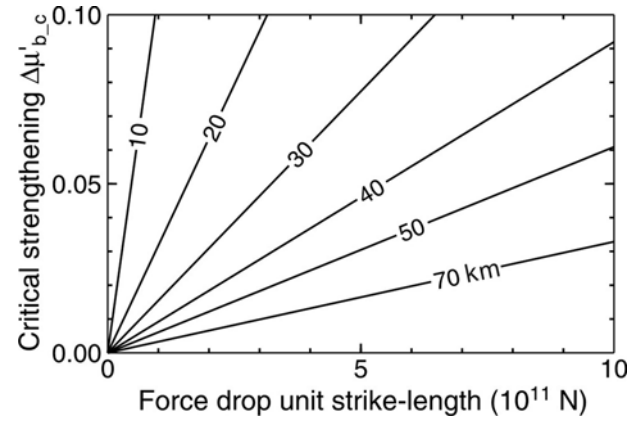

Figure 6. Relation of the critical strengthening $\Delta\mu'_{b\_c}$ of the updip zone with the force drop ΔF over the seismogenic zone. Given trench-normal width (km) of the shallowest updip aseismic segment (labeled on each line), $\Delta\mu'_{b\_c}$ scales linearly with ΔF.

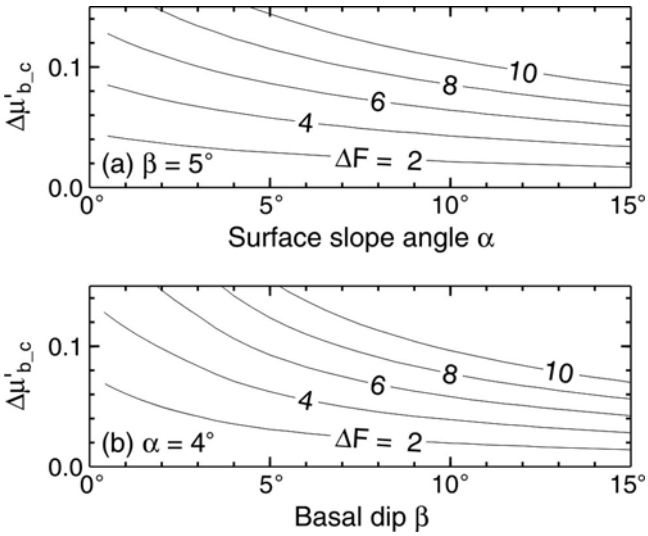

Figure 7. Effects of wedge geometry on the critical strengthening $\Delta\mu'_{b\_c}$ of an updip zone of 30 km horizontal width. (a) Effects of surface slope angle α for a fixed basal dip $\beta = 5°$. (b) Effects of β for a fixed $\alpha = 4°$. Each curve represents a model with the labeled force drop $\Delta F(\times 10^{11}$ N) along the seismogenic zone per unit strike length.

Table 1. Surface Slope Angle (α, ±1°), Basal Dip (β, ±2°), and Trench-Normal Width of Outer Wedges at Accretionary Subduction Margins

Name	Location[a]	Width (km)	α	β	Source
Barbados	15°30′N, 58°40′W	25	2.3	2.2	*Moore et al.* [1995]
Nankai	33°N, 136°50′E	30	4.0	5.8	*Park et al.* [2002], *von Huene and Ranero* [2003], *Bangs et al.* [2006]
	32°20′N, 134°40′E	35	3.5	3.6	*Park et al.* [2002], *von Huene and Ranero* [2003], *Bangs et al.* [2006]
Alaska	57°30′N, 147°50′W	25	3.5	2.4	*von Huene and Ranero* [2003], *von Huene and Klaeschen* [1999], *Fruehn et al.* [1999]
	59°10′N, 145°50′W	25	8.7	4.7	*von Huene and Ranero* [2003], *von Huene and Klaeschen* [1999], *Fruehn et al.* [1999]
Aleutian	54°10′N, 157°20′W	35	4.0	5.9	*Bruns and von Huene* [1986], *Scholl et al.* [1986]
	50°30′N, 175°W	35	5.0	8.2	*Bruns and von Huene* [1986], *Scholl et al.* [1986]
S. Chile	33°10′S, 72°40′W	25	5.6	7.4	*von Huene and Ranero* [2003], *Laursen et al.* [2002]
Sunda	6°50′S, 102°10′E	40	4.6	4.5	*Kopp and Kukowski* [2003]
	8°S, 104°E	35	3.6	4.3	*Kopp and Kukowski* [2003]
	9°10′S, 106°20′E	40	4.4	5.9	*Kopp and Kukowski* [2003]
N. Cascadia	47°20′N, 125°30′W	15	2.1	2.4	*Flueh et al.* [1998]
S. Cascadia	44°40′N, 125°20′W	20	7.2	4.7	*Snavely et al.* [1986], *Gerdom et al.* [2000]
Kurile	43°N, 148°20′E	30	3.6	5.5	*Klaeschen et al.* [1994], *Schnürle et al.* [1995]
Kermadec	26°20′S, 175°20′W	30	3.0	8.8	*von Huene and Scholl* [1991]
C. Hikurangi	39°20′S, 178°40′W	>15	0.9	3.2	P. Barnes (personal communication, 2006)
S. Hikurangi	41°S, 178°W	35	1.5	4.5	*Davey et al.* [1986]
Makran	24°10′N, 62°50′E	30	2.0	4.4	*Kopp et al.* [2000], *Kukowski et al.* [2001]

[a]Location is where the profile crosses the trench.

[2006], parameter $\mu_b'/(1-\lambda)$ was called the effective friction coefficient and denoted μ_b'. On the basis of (2) and a more general solution for an elastic wedge by *Hu and Wang* [2006], all stress components normalized by $\rho g y$ (e.g., $\bar{\sigma}_x' = \bar{\sigma}_x/\rho g y$) can be written as

$$\bar{\sigma}_x' = -m(1-\lambda)\cos\alpha \tag{3a}$$

$$\bar{\sigma}_y' = -(1-\lambda)\cos\alpha \tag{3b}$$

$$\tau_{xy}' = (1-\rho')\sin\alpha \tag{3c}$$

where $\rho' = \rho_w/\rho$, and m is called the effective stress ratio.

[23] The effective stress ratio m determines whether the wedge is stable (elastic deformation) or critical (at Coulomb failure). For a wedge of fixed geometry and material strength, this parameter has two critical values, denoted m^c, with which the wedge is in a critical state [*Wang and Hu*, 2006]. The smaller m^c, corresponding to a weaker basal fault, represents an extensionally critical state in which the wedge is everywhere on the verge of gravitational collapse. The larger m^c, corresponding to a stronger fault, represents a compressively critical state in which the wedge is everywhere on the verge of compressive failure. For any m value between these two m^c values, the wedge is in a stable state and undergoes elastic deformation. Given wedge geometry, m is a function of μ_b' and λ. Expressions for m for both the stable and critical states were given by *Wang and Hu* [2006]. Because of the above mentioned change of mathematical symbols for the effective coefficient and related parameters, we rewrite their expressions in Appendix B using the new symbols adopted in this paper. A change in μ_b' and/or λ results in a change in m and thus may cause the wedge to switch between stable and critical states. Repeated Coulomb failure of the wedge material over geological times gradually shapes the wedge taper.

Table 2. Surface Slope Angle (α, ±1°), Basal Dip (β, ±2°), and Trench-Normal Width of Outer Wedges at Erosional Subduction Margins

		Frontal Prism			Middle Prism			
Name	Location[a]	Width (km)	α	β	Width (km)	α	β	Source
Costa Rica	9°40′N, 86°10′W	5	7.4	4.9	30	4.5	7.2	*Ye et al.* [1996], *Christeson et al.* [1999], *Ranero et al.* [2008]
	9°10′N, 85°40′W	10	5.0	3.8	30	3.0	5.9	*Ye et al.* [1996], *Christeson et al.* [1999], *Ranero et al.* [2008]
	8°50′N, 85°30′W	8	5.0	4.8	15	5.9	5.6	*Ye et al.* [1996], *Christeson et al.* [1999], *Ranero et al.* [2008]
N. Chile	23°20′S, 71°20′W	15	8.5	5.5	35	4.2	10.0	*Sallarès and Ranero* [2005]
Ryukyu	25°20′N, 128°20′E	<5			30	4.9	5.8	*Kodaira et al.* [1996]
Ecuador	3°20′N, 79°W	10	5.5	6.1	20	4.5	5.2	*Collot et al.* [2004], B. Marcaillou (personal communication, 2008)
Tonga	23°30′S, 174°50′W	<3			30	9.3	10.0	*von Huene and Scholl* [1991]
Guatemala	13°N, 91°W	<3			45	5.8	9.0	*Aubouin et al.* [1984]
Nicaragua	11°20′N, 87°30′W	<5			25	7.1	6.3	*Ranero et al.* [2000]
S. Sandwich	~57°S, 24°30′W	5			20	9.2	10.0	*Vanneste and Larter* [2002]
NE Japan	40°5′N, 144°20′E	5	7.4	11.7	10	7.1	12.6	*von Huene et al.* [1986]
	39°40′N, 144°20′E	<10	8.1	4.6	25	4.7	5.5	*von Huene et al.* [1994]
Peru	8°30′S, 81°W	15	7.9	5.5	35	5.0	8.3	*Krabbenhöft et al.* [2004]
	11°40′S, 79°10′W	15	9.1	3.5	30	3.0	5.3	*Krabbenhöft et al.* [2004]
	13°30′S, 78°W	15	6.9	4.8	50	2.8	8.7	*Krabbenhöft et al.* [2004]
Mexico	15°50′N, 99°W	<3			20	8.6	2.0	*Collins and Watkins* [1986]

[a]Location is where the profile crosses the trench.

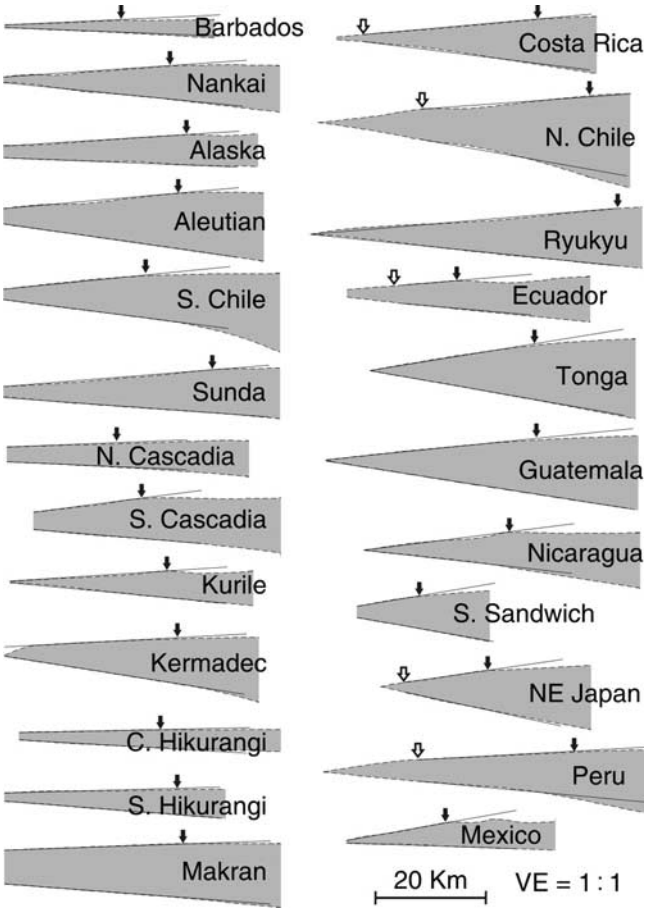

Figure 8. Observed geometry of subduction zone wedges based on published seismic sections referenced in Tables 1 and 2 (shaded area with dashed outline) and linear approximations of their upper and lower surfaces used in this work (solid lines). (left) Accretionary margins and (right) predominantly erosional margins. The transition between outer and inner wedges for each margin is approximately marked by a solid arrow. For erosional margins, where a frontal sedimentary prism can be clearly discerned on the seismic section, the limit of the prism is marked by a hollow arrow. If there are multiple seismic sections, only one of them is shown here. There is no vertical exaggeration.

3.2. Observed Geometry of Outer Wedges

[24] In order to apply wedge mechanics and what we learned from the stress transfer modeling to real subduction zones, we compiled published seismic survey depth sections and measured the geometry of the outer wedge for 22 margins. We first determined the location of the transition of the outer and inner wedges on the basis of the deformation pattern of the fore arc as described by the authors who published these sections as well as a surface slope break. An outer wedge shows active permanent deformation and evidence for out-of-sequence faults, and its surface slope is usually steeper than that of the inner wedge. We then drew linear outlines to approximate the outer-wedge surface and the subduction interface and determined α and β from these straight lines (Tables 1 and 2). Figure 8 compares the outlines of the observed geometry (dashed lines) and our linear approximations (solid lines). Where there are several seismic survey profiles less than 100 km apart, we studied all the profiles but only present an average of these measurements. For most margins, we show only one representative profiles in Figure 8. Obviously, the slope of the seafloor is generally more accurately determined than the dip of the subduction fault in seismic sections. Considering the uncertainties in the traveltime to depth conversion in published papers and in the measurements in this work, we estimate the errors in α and β to be at least $\pm 1^\circ$ and $\pm 2^\circ$, respectively. Additionally, along-strike variations in α often exceed measurement uncertainties from a single profile, and it should be cautioned that the geometry determined from a single profile may not represent the along-strike average.

[25] Measurements of α and β involving different trench-normal distances may yield different results. For example, for one of the profiles contributing to the first suite of average Nankai values listed in Table 1, we obtained $\alpha = 4.5^\circ$ and $\beta = 5.3^\circ$ for an outer wedge of 20 km width. For the same profile, *Lallemand et al.* [1994] obtained $\alpha = 4.0^\circ$ and $\beta = 5.5^\circ$ for a wedge of 40 km width by measuring a segment from the trench to a position corresponding to a decollement depth of 10 km below seafloor. Surface slope values reported by *Lallemand et al.* [1994] for various subduction zones are generally slightly smaller than ours, because all their measurements were made over a larger region including the most seaward part of the inner wedge.

[26] Our measurements of accretionary outer wedge sections (Table 1) give an average surface slope angle $\alpha = 3.9^\circ$ and basal dip $\beta = 4.9^\circ$. It is interesting to note that most of the recent devastating megathrust earthquakes of M_w 9 or greater have occurred at accretionary margins, such as the 1700 Cascadia, 1960 Chile, 1964 Alaska, and 2004 Sumatra earthquakes. Overall, outer wedges of margins that produced large megathrust earthquakes, such as Alaska, southern Chile, southwestern Japan, and southern Cascadia (Oregon), feature larger surface slope angles, comparing to those with smaller megathrust earthquakes, such as Barbados, Kurile, Kermadec, and Hikurangi. This suggests a connection between outer wedge geometry and megathrust earthquakes, although there are also exceptions. At some accretionary margins of very large sediment supply, such as northern Cascadia [*Flueh et al.*, 1998] and Makran [*Kopp et al.*, 2000; *Kukowski et al.*, 2001], between the deformation front and the point where the surface slope sharply steepens and seismic reflectors in the sediments suddenly become disordered is a section of very thick, nearly horizontally layered oceanic sediments ($\geq$2 km). In this work, we assume that the outer wedge at these margins start from where the surface slope sharply steepens.

[27] Outer wedges at some erosional margins, such as Costa Rica, North Chile, and Peru, include a frontal prism consisting mainly of land-derived debris and a middle prism consisting mainly of the rock frame of the upper plate (Figures 1c and 8). Where possible, we have measured the geometry of both the frontal and middle prisms. The surface slope of the frontal prism is generally steeper than that of the middle prisms (Figure 9). Excluding the frontal prisms, our measurements of erosional outer wedges (Table 2) give an average $\alpha = 5.6^\circ$ and $\beta = 7.3^\circ$.

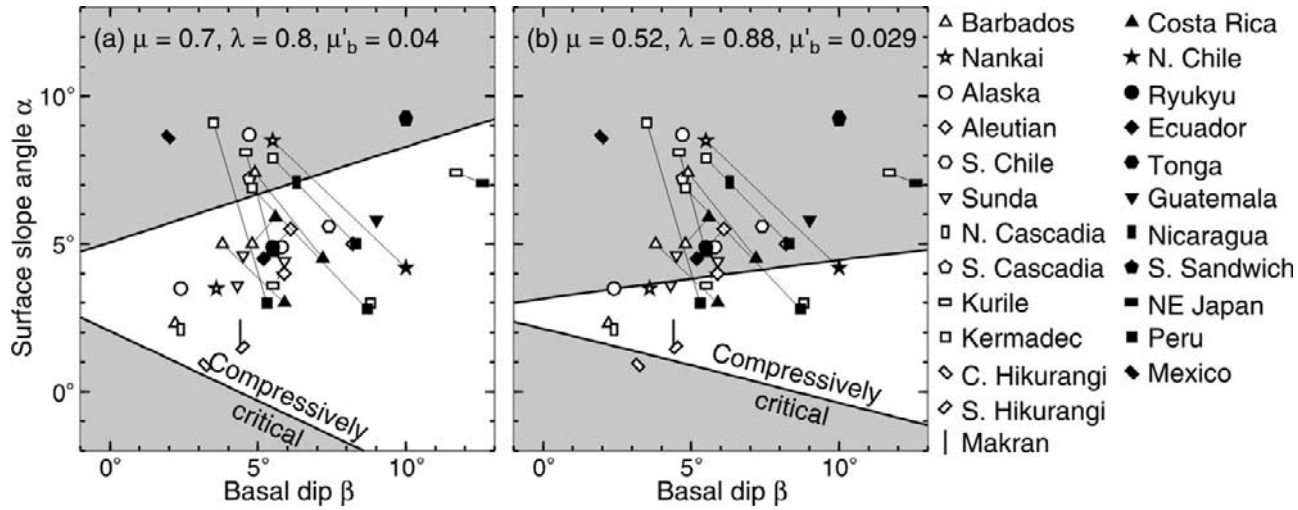

Figure 9. Surface slope angle α versus basal dip β for outer wedges of 22 subduction zones compared with Coulomb wedge models. (a) Comparison with the reference wedge model. (b) Comparison with the weak wedge model of *Lallemand et al.* [1994]. Isolated open and solid symbols represent accretionary and erosional margins, respectively. For erosional margins where frontal prisms are wider than 10 km, the middle prism (solid symbol) and the frontal prism (open symbol) are both shown and linked with a thin line. The pair of thick solid lines brackets the stable region of a Coulomb wedge model with the shown set of material parameters. The top one of the pair represents extensionally critical states (on the verge of gravitational collapse), and the bottom one represents compressively critical states.

[28] In Figure 9a, we compare the geometry measurements with a reference wedge model using the Coulomb wedge theory. For the reference wedge model, we assume an internal friction coefficient $\mu = 0.7$ [*Wang and Hu*, 2006], internal pore fluid pressure ratio $\lambda = 0.8$, and basal effective friction coefficient $\mu_b' = 0.04$ (the same as that of the updip zone in the interseismic phase assumed in section 2). Accretionary outer wedges accumulate materials and deform by compressive failure and therefore are expected to be compressively critical. Erosional outer wedges must also be overall compressively critical, although they may sometimes become extensionally critical in an extremely relaxed state in great earthquake cycles (K. Wang et al., unpublished data, 2008). Therefore, each data point in Figure 9 is expected to be on a line of compressively critical states similar to the lower solid trajectories shown in Figure 9. However, Figure 9a would indicate that the outer wedges of most subduction zones are in a stable state (white area). For the weak wedge model of *Lallemand et al.* [1994] shown in Figure 9b, most wedges would be stable or gravitationally unstable. Figure 9 indicates that, with reasonable parameter values, the steady state Coulomb wedge theory cannot fully explain the mechanics of outer wedges.

3.3. Application of Wedge Mechanics to Outer Wedges

[29] How do we make the outer wedges compressively critical, that is, how to move the line of the compressively critical states in Figure 9a or 9b upward? We vary parameter values of the reference wedge model to illustrate their roles in achieving this goal. For each plot of Figure 10, the solid trajectories represent the reference wedge model in Figure 9a, and the dashed trajectories represent a model with one or more parameters being different from the reference model. The models of a weaker wedge, either with a smaller internal friction coefficient $\mu = 0.6$ (Figure 10a) or a greater

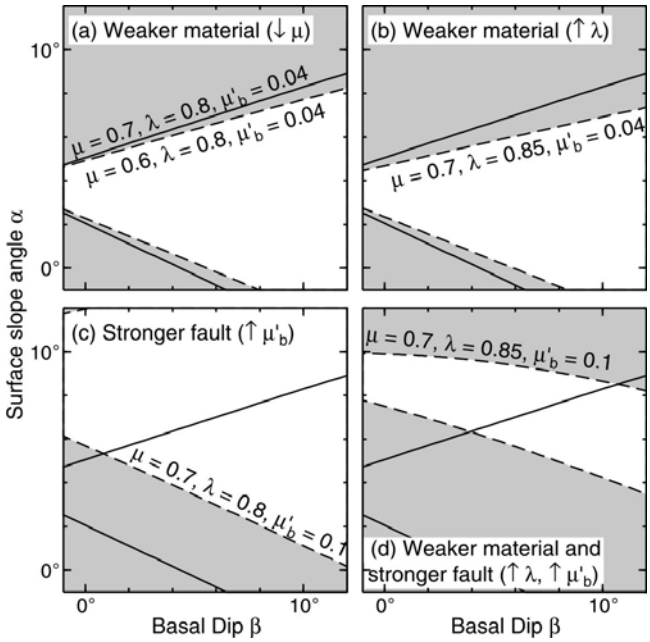

Figure 10. Surface slope angle α versus basal dip β for models with different parameter combinations (labeled on the critical state trajectories). Solid lines represent the reference wedge model shown in Figure 9a. Dashed lines dividing stable (white) and unstable (shaded) regions are critical state trajectories of models with one or two parameters different from the reference model. (a) Effects of a weaker wedge due to a smaller μ. (b) Effects of a weaker wedge due to a greater λ. (c) Effects of a stronger basal fault due to a greater μ_b'. (d) Combined effects of a stronger basal fault (greater μ_b') and a weaker wedge (greater λ).

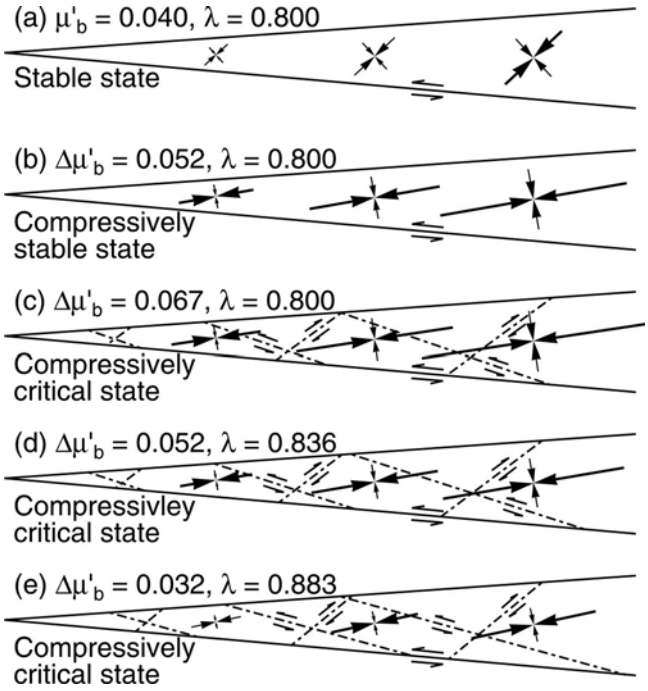

Figure 11. Stress field in a wedge with $\alpha = 4°$, $\beta = 5°$, and $\mu = 0.7$ for different λ and μ_b' values as labeled. (a) A compressively stable wedge representing the interseismic stage. (b) With coseismic strengthening of the basal fault $\Delta\mu_b' = 0.052$ (i.e., $\mu_b' = 0.092$) but without increasing pore fluid pressure ratio λ, the wedge is still compressively stable. (c) With greater coseismic strengthening $\Delta\mu_b' = 0.067$ (i.e., $\mu_b' = 0.107$) and without increasing λ, the wedge is compressively critical. (d) With moderate strengthening $\Delta\mu_b' = 0.052$ and an increase in λ, the wedge is compressively critical. (e) With a low degree of strengthening $\Delta\mu_b' = 0.032$ (i.e., $\mu_b' = 0.072$) but a greater increase in λ, the wedge is compressively critical. Dot-dashed lines in Figures 11c, 11d, and 11e represent potential faulting directions.

internal pore fluid pressure ratio $\lambda = 0.85$ (Figure 10b) move the line of compressively critical states slightly upward. The model of a stronger basal fault with friction $\mu_b' = 0.1$ (Figure 10c) moves it upward significantly. The combined effect of a weaker wedge and a stronger basal fault is even greater (Figure 10d). Therefore, a model with a stronger basal fault (larger μ_b') and/or a weaker wedge (smaller μ and/or larger λ) is required to drive an outer wedge toward compressive failure. As discussed in section 2, a stronger basal fault can be achieved through coseismic strengthening.

[30] In the following, we discuss how the moderate coseismic strengthening discussed in section 2 can drive the outer wedge into a compressively critical state. For our model wedge, we assume $\alpha = 4°$ and $\beta = 5°$, the same as for the stress transfer model shown in Figure 3a and similar to the observed average geometry of the accretionary outer wedges shown in Figure 9. The model shown in Figure 11a is the reference wedge model, with material property values given in Figure 9a, for the specified geometry. For an interseismic strength of the basal fault $\mu_b' = 0.04$, the outer wedge is stable as shown in Figure 11a, similar to those falling in the white region of Figure 8a for a wide range of wedge geometry.

[31] With the strength of the wedge material fixed, a strengthening of the updip zone of the basal fault by $\Delta\mu_b' = 0.052$ as in the reference earthquake model (Figure 4, solid lines) is not sufficient to push the outer wedge into a compressively critical state (Figure 11b). By simply strengthening the basal fault alone, a critical wedge of the given geometry and material properties requires an increase in fault strength by $\Delta\mu_b' = 0.067$ (Figure 11c), greater than that of the reference earthquake by a factor of 1.3. Figure 6 (the 30 km line) shows that this requires the force drop of the earthquake to be greater by at least the same factor, by increasing either the stress drop or downdip width of the seismogenic zone.

[32] An earthquake not only causes strengthening of the updip fault zone, but also causes weakening of the wedge material because coseismic compression of the outer wedge leads to an increase in its internal pore fluid pressure [*Wang and Hu*, 2006]. As shown in Figure 10d, a combination of fault strengthening and wedge weakening has a much greater tendency to make the wedge critical than does fault strengthening alone. For example, for the reference earthquake shown in Figure 4 (solid lines), the wedge will become compressively critical if the wedge material is weakened by coseismically increasing λ to 0.836 (Figure 11d). The amount of increase from 0.8 to 0.836 shown here is an arbitrarily assumed scenario for the purpose of illustrating the point. Given $\Delta\mu_b'$, the increase in λ required to bring the wedge into a critical state depends on the initial value of λ. For example, if λ is initially 0.835, an increase of merely 0.001 will suffice. Even for the model earthquake of a much lesser degree of strengthening of $\Delta\mu_b' = 0.032$, shown using dashed lines in Figure 4b, increasing λ to 0.883 can also result in a compressively critical wedge (Figure 11e). The comparison between Figures 11d and 11e illustrates the trade-off between $\Delta\mu_b'$ and λ.

[33] The fundamental mechanics of the results displayed in Figure 11 can be better explained using the effective

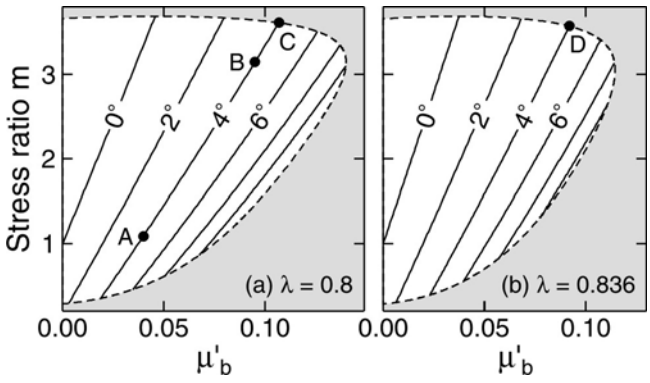

Figure 12. Stress ratio m as a function of effective friction coefficient μ_b' for wedges with $\beta = 5°$ and $\mu = 0.7$ but different α values. (a) Internal pore fluid pressure ratio $\lambda = 0.8$. (b) Internal pore fluid pressure ratio $\lambda = 0.836$. The dashed trajectory representing critical states divides areas of stable states (white) and unstable states (shaded). Stresses for states A, B, C, and D are illustrated in Figures 11a, 11b, 11c, and 11d, respectively.

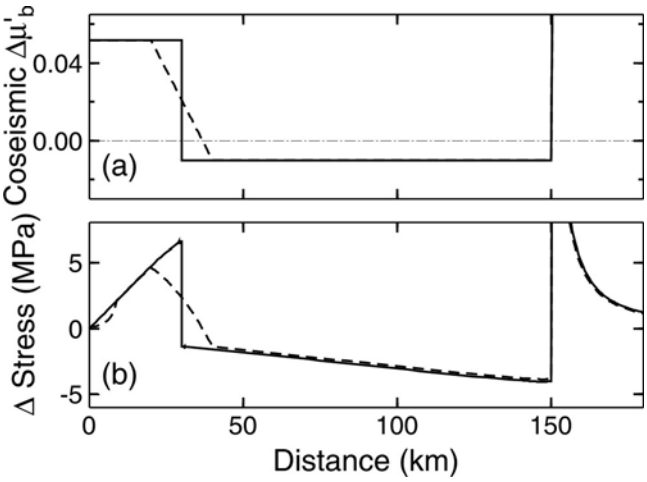

Figure 13. An example (dashed line) illustrating the effects of a more gradual change in fault friction than assumed for the reference earthquake model shown in Figure 4 (reproduced here also using solid lines). (a) Coseismic strength change $\Delta\mu_b'$ along the fault. (b) Shear stress change along the fault.

stress ratio m (equation (3)). Still with $\beta = 5°$, $\lambda = 0.8$, and $\mu = 0.7$, we show m as a function of the effective friction coefficient μ_b' in Figure 12a for different α values, using expressions of m given in Appendix B. Given α, the stress ratio varies along a nearly straight line in the stable area in response to changes in basal fault friction. Points A and B along the line of $\alpha = 4°$ represent the stable states shown in Figures 11a and 11b, respectively, and point C represents the critical state shown in Figure 11c. In a somewhat speculative scenario, if several earthquakes occur sequentially in the same area, and the stress induced by each event does not fully relax, the wedge may gradually evolve from state A to state C because of the cumulative effects of these earthquakes. Without coseismically increasing λ, a coseismic fault strengthening of $\Delta\mu_b' = 0.052$ will move the wedge from state A to state B. With an increase of λ to 0.836 as well, the same earthquake theoretically moves the wedge from state A in Figure 12a to the compressively critical state D in Figure 12b (with stresses displayed in Figure 11d).

4. Discussion

4.1. Coseismic Strengthening Greater Than $\Delta\mu_{b\_c}'$

[34] In section 3, we have examined the effects of an earthquake rupture on the outer wedge assuming the entire updip zone of the fault is at Coulomb failure, that is, its coseismic strengthening is equal to or less than $\Delta\mu_{b\_c}'$. If the strengthening is greater than $\Delta\mu_{b\_c}'$, the increase in shear stress takes place mainly in the deeper portion of the updip zone, and the shallower portion is in a stress shadow (e.g., models represented by dotted lines in Figure 4). The localized large shear stress increase is expected to bring two effects. First, it may cause localized compression and permanent deformation of the overlying wedge material. Repeated occurrences of the localized permanent deformation may explain the presence of an outer ridge between the outer wedge and inner wedge at some subduction zones such as Tonga. Second, relaxation of the large shear stress in this region after the earthquake may result in a delayed stress transfer to the shallower part of the updip zone that was in the stress shadow during the earthquake. This may gradually and temporarily increase compression in the more frontal part of the outer wedge. The timescale of the delayed stress transfer is an interesting subject for future research.

4.2. Transitional Change of $\Delta\mu_b'$ Between the Strengthening and Weakening Segments

[35] In a real subduction zone, the frictional property of the megathrust is likely to change more gradually between the updip and the seismogenic zones than portrayed by our simplified model shown in Figure 2. To demonstrate the effect of a more gradual change, we compare the reference earthquake model with a model in which the strengthening of the updip zone ($\Delta\mu_b' > 0$) linearly changes to the weakening of the seismogenic zone ($\Delta\mu_b' < 0$) over a horizontal distance of 20 km (Figure 13a). Other model parameters are the same as for the reference earthquake model. The transitional change of $\Delta\mu_b'$ leads to a stress change that is less abrupt than in the reference earthquake model (Figure 13b). The addition of this transition makes the seismogenic zone slightly narrower, and the resultant smaller force drop in the seismogenic zone is unable to push the updip zone into complete failure given the same degree of strengthening. Except for these minor details, the abrupt changes in $\Delta\mu_b'$ assumed in section 2 do not significantly bias the results. However, in reality, the more gradual stress change may result in a more gradual change in the topography between the outer and inner wedges over numerous earthquake cycles. In some accretionary margins, such as Alaska, Barbados, and Kurile (Figure 8), the surface slope angle of the outer wedge changes to the smaller value of the inner wedge indeed very gradually.

5. Conclusions

[36] The recognition that stress increase along the shallowest part of the subduction fault during a great earthquake must cause greater compression in the overlying wedge led to the dynamic Coulomb wedge concept [*Wang and Hu*, 2006]: the outer wedge tends to enter a compressively critical state and endure permanent deformation mainly during great earthquakes. In the present work, we address a key component of this process, that is, how and how much stress is transferred from the seismogenic zone to the updip zone during an earthquake. To simplify the problem, we have modeled the process of coseismic stress transfer separately from Coulomb wedge deformation and apply the model results to wedge mechanics.

[37] Our static finite element model of stress transfer includes two converging elastic plates in contact along a subduction fault with effective friction coefficient μ_b'. A decrease in μ_b' is applied to the seismogenic zone of the fault to simulate weakening in an earthquake, and an increase in μ_b' is applied to the updip zone to simulate strengthening. The wealth of model behavior can be characterized by examining the critical strengthening, $\Delta\mu_{b\_c}'$, of the updip

zone, which is the minimum strengthening required to prevent the rupture from breaking the trench. If the strengthening is equal to or less than $\Delta\mu'_{b\_c}$, the entire updip zone is at failure. If the strengthening is greater than $\Delta\mu'_{b\_c}$, only the deeper part of the updip zone fails. Given geometry and rigidity structure, $\Delta\mu'_{b\_c}$ is a linear function only of the force drop ΔF, defined as the product of the average stress drop and the area of the seismogenic zone. For the same ΔF, a narrower outer wedge requires a higher degree of $\Delta\mu'_{b\_c}$ to resist rupture.

[38] We have compiled observations of wedge geometry from 22 subduction zones and have found that the surface slope is generally too high to be explained by steady state Coulomb wedge models. The high-slope angles require rather high basal stress and/or weak wedge material. Our stress transfer models have demonstrated that the high stress in the shallow part of the subduction zone can be readily achieved in great earthquakes. We further reason that a slight increase in pore fluid pressure within the compressed wedge can coseismically weaken the wedge material. The combined effects of a stronger fault and a weaker wedge can readily bring the wedge into a compressively critical state. Repeated occurrences of great earthquakes can control the overall geometry of the outer wedge over the geological timescale.

Appendix A: Comparison of Our Stress Transfer Model With the Dislocation Model and Crack Model

[39] Temporal and spatial changes in friction cause stress drop and increase along the subduction fault during earthquakes. The stress changes control coseismic slip distribution along the fault, and the fault motion induces deformation on the ground surface. Depending on the purpose of research, different models can be used to model different aspects of this process. Dislocation models are widely used to model crustal deformation by kinematically prescribing coseismic slip along the fault without considering realistic stress changes. Crack models are often used to model coseismic fault slip and resultant surface deformation by prescribing a stress drop in the rupture zone independent of the initial stress and without considering how the stress drop is controlled by changes in fault friction. Our stress transfer model prescribes a change in fault friction and calculates the resultant stress change from an initial state and the consequent fault slip and surface deformation.

[40] Here we compare these three approaches using simple models: a uniform-slip dislocation model, a uniform-stress drop crack model, and a uniform-friction change stress transfer model. In this comparison, we assume a linear subduction fault dipping at 15° in an elastic half-space, with the seismogenic zone extending from 30 km to 150 km from the trench (Figure A1a). Vertical and horizontal dimensions are made very large to approximate the half-space assumption. Parameters are chosen so that the thrust earthquakes simulated using the three models have the same seismic moment.

[41] For the uniform-slip dislocation model, we use the analytical solution of *Okada* [1992] for a buried rectangular fault. The 2-D results (dotted line in Figure A1d) are obtained by assuming an extremely large strike length for the rectangular fault. Stress changes along the fault associated with the deformation are then determined from the calculated strain. The prescribed discontinuous slip along the subduction fault results in stress singularities at the updip and downdip edges of the rupture zone.

[42] The crack model is readily simulated by modifying our finite element stress transfer model, although there are various more precise analytical and numerical solutions [*Rudnicki and Wu*, 1995; *Geist and Dmowska*, 1999]. To produce a uniform stress drop in the rupture zone, we need to device a variable $\Delta\mu'_b$ (dashed line in Figure A1b). To prevent any slip beyond the rupture zone, a situation portrayed by the most conventional crack model, we simply assign very large $\Delta\mu'_b$ values to the updip and downdip zones. In the uniform-stress drop crack model, fault slip at the edges of the rupture zone is continuous, but the stress is singular, although the singularity is milder than in the uniform-slip dislocation model. Numerically, we have approximated the singularity behavior with a very sharp stress gradient handled using very small elements.

[43] For the stress transfer model, a uniform $\Delta\mu'_b = -0.006$ is applied to the seismogenic zone to produce an averaged stress drop of 4 MPa, and a strengthening of $\Delta\mu'_b = 0.042$ is assigned to the updip zone. Coseismic slip can extend into the updip zone (solid line in Figure A1d). The termination of the slip updip of the seismogenic zone is more gradual than in the crack model and is not accompanied with a stress singularity. For simplicity, we have purposely made the downdip termination of the slip identical to that of the crack model. In reality, the termination should be in a gradual fashion similar to the updip termination.

[44] The three models produce similar surface deformation patterns over the downdip edge of the rupture zone and farther away from the trench. Because the downdip edge is rather deeply buried, surface deformation is not very sensitive to the details of the slip termination. However, the manner of the slip termination around the more shallowly buried updip end of the seismogenic zone has a greater impact on surface deformation, with the most abrupt termination (the uniform-slip dislocation model) producing the largest localized uplift.

Appendix B: Expressions for the Effective Stress Ratio *m*

[45] The effective coefficient of friction μ'_b (equation (2)) was referred to as a basal friction property and denoted μ''_b in the paper by *Wang and Hu* [2006]. In the same paper, and also in papers by *Dahlen* [1984], *Wang et al.* [2006], and most other publications on the development and application of the Coulomb wedge theory, parameter $\mu'_b/(1-\lambda)$ was referred to as the effective coefficient of friction and denoted μ'_b. The naming and symbol systems adopted in the present paper are more consistent with the most commonly used definition of the effective coefficient of friction for a fault, that is, the ratio of the normal and shear stresses at Coulomb failure. For example (see Figure 3b), for a subareal wedge ($\rho_w = 0$) with a small taper ($\theta = \alpha + \beta \approx 0$, so that $\sigma_n \approx \sigma_y$), $\bar{\sigma}_n/(1-\lambda) \approx \sigma_n$ and hence $\tau_n \approx \mu'_b\sigma_n$.

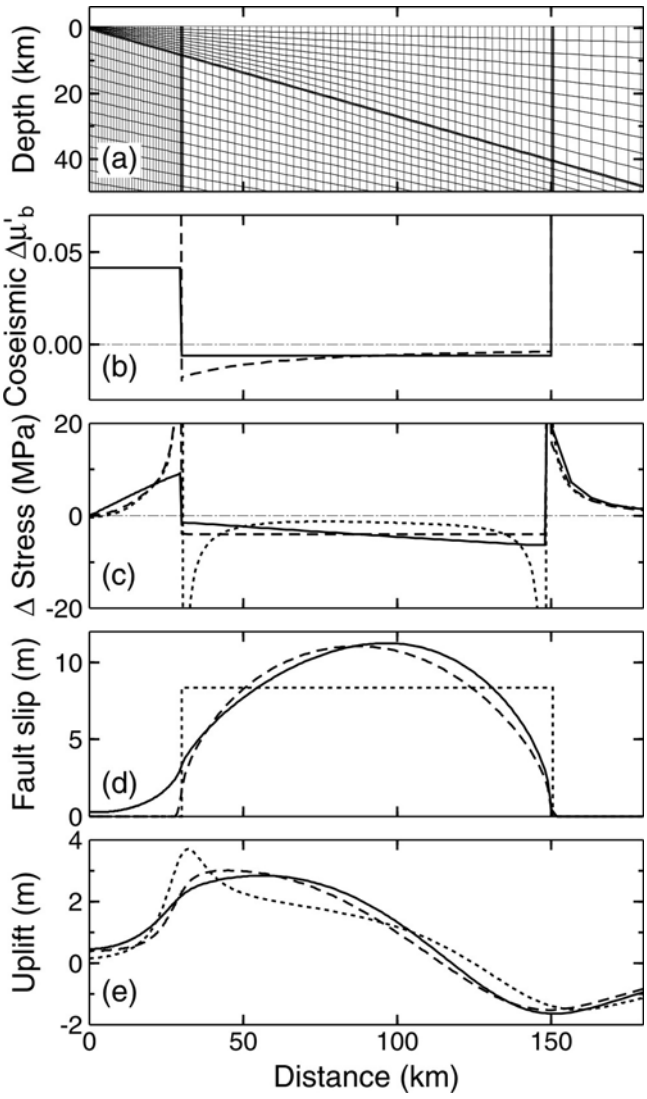

Figure A1. Comparison of our stress transfer model (solid line) with a uniform stress drop crack model (dashed line) and a uniform slip dislocation model (dotted line). The earthquakes simulated using the three models have the same moment magnitude. (a) Central part of the finite element mesh for the stress transfer and crack models. The "solid line" along the subduction fault and the two vertical solid lines bracketing the megathrust seismogenic zone are actually groups of densely spaced small elements. (b) Coseismic $\Delta\mu_b'$ along the fault (irrelevant to the dislocation model). (c) Stress drop (or increase) along the fault. (d) Slip distribution along the fault. (e) Vertical displacement at the surface.

Here we rewrite the expressions of the effective stress ratio m (equation (3)) given by *Wang and Hu* [2006] using the new symbol system. For a stable wedge

$$m = 1 + \frac{2\left((1-\lambda)\tan\alpha' + \mu_b'\right)}{\sin 2\theta\left(1-\lambda-\mu_b'\tan\theta\right)} - \frac{2\tan\alpha'}{\tan\theta} \qquad \text{(B1)}$$

where $\tan\alpha' = \frac{1-\rho'}{1-\lambda}\tan\alpha$. For a critical wedge

$$m^c = 1 + \frac{2(1+\eta)}{\csc\varphi\sec 2\psi_0^c - 1} \qquad \text{(B2)}$$

where $\varphi = \tan^{-1}\mu$ is the internal friction angle, ψ_0^c is the uniform angle between the most compressive principal stress σ_1 and the upper surface, and η is a dimensionless constant for cohesion S_0 defined as follows [*Wang and Hu*, 2006]

$$S_0 = \eta(1-\lambda)\mu\rho g y\cos\alpha \qquad \text{(B3)}$$

[46] **Acknowledgments.** We thank J. He for developing the finite element code used in this work and for his assistance in the stress transfer modeling. Comments from J.-P. Avouac, I. Manighetti, and an anonymous reviewer helped clarify a number of concepts. Y. Hu is supported by an NSERC postgraduate scholarship. Geological Survey of Canada contribution 20080281.

References

Aubouin, J., J. Bourgois, and J. Azéma (1984), A new type of active margin: The convergent-extensional margin, as exemplified by the Middle America Trench off Guatemala, *Earth Planet. Sci. Lett.*, *67*, 211–218, doi:10.1016/0012-821X(84)90116-X.

Baba, T., K. Hirata, T. Hori, and H. Sakaguchi (2006), Offshore geodetic data conducive to the estimation of the afterslip distribution following the 2003 Tokachi-oki earthquake, *Earth Planet. Sci. Lett.*, *241*, 281–292, doi:10.1016/j.epsl.2005.10.019.

Bangs, N. L. B., S. P. S. Gulick, and T. H. Shipley (2006), Seamount subduction erosion in the Nankai Trough and its potential impact on the seismogenic zone, *Geology*, *34*(8), 701–704, doi:10.1130/G22451.1.

Briggs, R. W., et al. (2006), Deformation and slip along the Sunda megathrust in the great 2005 Nias-Simeulue earthquake, *Science*, *311*, 1897–1901, doi:10.1126/science.1122602.

Bruns, T. R. and R. von Huene (1986), Aleutian Trench, Shumagin segment, seismic section 104, in *Seismic Images of Modern Convergent Margins Tectonic Structure*, edited by R. von Huene, *AAPG Stud. Geol.*, *26*, 14–19.

Christeson, G. L., K. D. McIntosh, T. H. Shipley, E. R. Flueh, and H. Goedde (1999), Structure of the Costa Rica convergent margin, offshore Nicoya Peninsula, *J. Geophys. Res.*, *104*(B11), 25,443–25,468, doi:10.1029/1999JB900251.

Clift, P., and P. Vannucchi (2004), Controls on tectonic accretion versus erosion in subduction zones: Implications for the origin and recycling of the continental crust, *Rev. Geophys.*, *42*, RG2001, doi:10.1029/2003RG000127.

Collins, B. P., and J. S. Watkins (1986), The Middle America Trench, in *Seismic Images of Modern Convergent Margins Tectonic Structure*, edited by R. von Huene, *AAPG Stud. Geol.*, *26*, 30–32.

Collot, J. Y., B. Marcaillou, F. Sage, F. Michaud, W. Agudelo, P. Charvis, D. Graindorge, M. A. Gutscher, and G. Spence (2004), Are rupture zone limits of great subduction earthquakes controlled by upper plate structures? Evidence from multichannel seismic reflection data acquired across the northern Ecuador–southwest Colombia margin, *J. Geophys. Res.*, *109*, B11103, doi:10.1029/2004JB003060.

Dahlen, F. A. (1984), Noncohesive critical Coulomb wedges: An exact solution, *J. Geophys. Res.*, *89*(B12), 10,125–10,133, doi:10.1029/JB089iB12p10125.

Davey, F. J., K. Lewis, J. R. Childs, and M. A. Hampton (1986), Convergent margin off east coast of North Island, New Zealand, parts I and II, in *Seismic Images of Modern Convergent Margins Tectonic Structure*, edited by R. von Huene, *AAPG Stud. Geol.*, *26*, 49–53.

Dieterich, J. H. (1992), Earthquake nucleation on faults with rate-dependent and state-dependent strength, *Tectonophysics*, *211*, 115–134, doi:10.1016/0040-1951(92)90055-B.

Flueh, E. R., et al. (1998), New seismic images of the Cascadia subduction zone from cruise SO108 - ORWELL, *Tectonophysics*, *293*, 69–84, doi:10.1016/S0040-1951(98)00091-2.

Fruehn, J., R. von Huene, and M. A. Fisher (1999), Accretion in the wake of terrane collision: The Neogene accretionary wedge off Kenai Peninsula, Alaska, *Tectonics*, *18*(2), 263–277, doi:10.1029/1998TC900021.

Geist, E. L., and R. Dmowska (1999), Local tsunamis and distributed slip at the source, *Pure Appl. Geophys.*, *154*, 485–512, doi:10.1007/s000240050241.

Gerdom, M., A. M. Trehu, E. R. Flueh, and D. Klaeschen (2000), The continental margin off Oregon from seismic investigations, *Tectonophysics*, *329*, 79–97, doi:10.1016/S0040-1951(00)00190-6.

Hsu, Y.-J., M. Simons, J.-P. Avouac, J. Galetzka, K. Sieh, M. Chlieh, D. Natawidjaja, L. Prawirodirdjo, and Y. Bock (2006), Frictional afterslip following the 2005 Nias-Simeulue earthquake, Sumatra, *Science*, *312*, 1921–1926, doi:10.1126/science.1126960.

Hu, Y., and K. Wang (2006), Bending-like behavior of wedge-shaped thin elastic fault blocks, *J. Geophys. Res.*, *111*, B06409, doi:10.1029/2005JB003987.

Hyndman, R. D., and K. Wang (1993), Thermal constraints on the zone of major thrust earthquake failure: The Cascadia subduction zone, *J. Geophys. Res.*, *98*(B2), 2039–2060, doi:10.1029/92JB02279.

Hyndman, R. D., M. Yamano, and D. A. Oleskevich (1997), The seismogenic zone of the subduction thrust faults, *Isl. Arc*, *6*, 244–260, doi:10.1111/j.1440-1738.1997.tb00175.x.

Kanamori, H. (1994), Mechanics of earthquakes, *Annu. Rev. Earth Planet. Sci.*, *22*, 207–237, doi:10.1146/annurev.ea.22.050194.001231.

Klaeschen, D., I. Belykh, H. Gnibidenko, S. Patrikeyev, and R. von Huene (1994), Structure of the Kuril Trench from seismic reflection records, *J. Geophys. Res.*, *99*(B12), 24,173–24,188, doi:10.1029/94JB01186.

Kodaira, S., T. Iwasaki, T. Urabe, T. Kanazawa, F. Egloff, J. Makris, and H. Shimamura (1996), Crustal structure across the middle Ryukyu trench obtained from ocean bottom sesimographic data, *Tectonophysics*, *263*, 39–60, doi:10.1016/S0040-1951(96)00025-X.

Kopp, C., J. Fruehn, E. R. Flueh, C. Reichert, N. Kukowski, J. Bialas, and D. Klaeschen (2000), Structure of the Makran subduction zone from wide-angle and reflection seismic data, *Tectonophysics*, *329*, 171–191, doi:10.1016/S0040-1951(00)00195-5.

Kopp, H., and N. Kukowski (2003), Backstop geometry and accretionary mechanics of the Sunda margin, *Tectonics*, *22*(6), 1072, doi:10.1029/2002TC001420.

Krabbenhöft, A., J. Bialas, H. Hopp, N. Kukowski, and C. Hübscher (2004), Crustal structure of the Peruvian continental margin from wide-angle seismic studies, *Geophys. J. Int.*, *159*, 749–764, doi:10.1111/j.1365-246X.2004.02425.x.

Kukowski, N., T. Schillhorn, K. Huhn, U. von Rad, S. Husen, and E. Flueh (2001), Morphotectonics and mechanics of the central Makran accretionary wedge off Pakistan, *Mar. Geol.*, *173*, 1–19, doi:10.1016/S0025-3227(00)00167-5.

Lallemand, S. E., P. Schnürle, and J. Malavieille (1994), Coulomb theory applied to accretionary and nonaccretionary wedges: Possible causes for tectonic erosion and/or frontal accretion, *J. Geophys. Res.*, *99*(B6), 12,033–12,055, doi:10.1029/94JB00124.

Laursen, J., D. W. Scholl, and R. von Huene (2002), Neotectonic deformation of the central Chile margin: Deepwater forearc basin formation in response to hot spot ridge and seamount subduction, *Tectonics*, *21*(5), 1038, doi:10.1029/2001TC901023.

Liu, Y., and J. R. Rice (2007), Spontaneous and triggered aseismic deformation transients in a subduction fault model, *J. Geophys. Res.*, *112*, B09404, doi:10.1029/2007JB004930.

Manighetti, I., M. Campillo, C. Sammis, P. M. Mai, and G. King (2005), Evidence for self-similar, triangular slip distributions on earthquakes: Implications on earthquake and fault mechanics, *J. Geophys. Res.*, *110*, B05302, doi:10.1029/2004JB003174.

Marone, C. J., C. H. Scholz, and R. Bilham (1991), On the mechanics of earthquake afterslip, *J. Geophys. Res.*, *96*(B5), 8441–8452, doi:10.1029/91JB00275.

Moore, G. F., Z. Zhao, T. H. Shipley, N. Bangs, and J. C. Moore (1995), Structural setting of the Leg 156 area, northern Barbados Ridge accretionary prism, *Proc. Ocean Drill. Program, Initial Rep.*, *156*, 13–27.

Okada, Y. (1992), Internal deformation due to shear and tensile faults in a half-space, *Bull. Seismol. Soc. Am.*, *82*, 1018–1040.

Park, J. O., T. Tsuru, S. Kodaira, P. R. Cummins, and Y. Kaneda (2002), Splay fault branching along the Nankai subduction zone, *Science*, *297*, 1157–1160.

Ranero, C. R., R. von Huene, E. Flueh, M. Duarte, D. Baca, and K. McIntosh (2000), A cross section of the convergent Pacific margin of Nicaragua, *Tectonics*, *19*(2), 335–357, doi:10.1029/1999TC900045.

Ranero, C. R., I. Grevemeyer, H. Sahling, U. Barckhausen, C. Hensen, K. Wallmann, W. Weinrebe, P. Vannucchi, R. von Huene, and K. McIntosh (2008), Hydrogeological system of erosional convergent margins and its influence on tectonics and interplate seismogenesis, *Geochem. Geophys. Geosyst.*, *9*, Q03S04, doi:10.1029/2007GC001679.

Rudnicki, J. W., and M. Wu (1995), Mechanics of dip-slip faulting in an elastic half-space, *J. Geophys. Res.*, *100*(B11), 22,173–22,186, doi:10.1029/95JB02246.

Ruina, A. (1983), Slip instability and state variable friction law, *J. Geophys. Res.*, *88*(B12), 10,359–10,370, doi:10.1029/JB088iB12p10359.

Sallarès, V., and C. R. Ranero (2005), Structure and tectonics of the erosional convergent margin off Antofagasta, north Chile (23°30′S), *J. Geophys. Res.*, *110*, B06101, doi:10.1029/2004JB003418.

Schnürle, P., S. E. Lallemand, R. von Huene, and D. Klaeschen (1995), Tectonic regime of the southern Kurile Trench as revealed by multichannel seismic lines, *Tectonophysics*, *241*, 259–277, doi:10.1016/0040-1951(94)00173-7.

Scholl, D. W., J. McCarthy, and H. Ryan (1986), Forearc margin, central Aleutian Ridge, in *Seismic Images of Modern Convergent Margins Tectonic Structure*, edited by R. von Huene, *AAPG Stud. Geol.*, *26*, 10–13.

Snavely, P. D., Jr., R. von Huene, D. M. Mann, and J. Miller (1986), The central Oregon continental margin, lines WO76–4 and WO76–5, in *Seismic Images of Modern Convergent Margins Tectonic Structure*, edited by R. von Huene, *AAPG Stud. Geol.*, *26*, 24–29.

Vanneste, L. E., and R. D. Larter (2002), Sediment subduction, subduction erosion, and strain regime in the northern South Sandwich forearc, *J. Geophys. Res.*, *107*(B7), 2149, doi:10.1029/2001JB000396.

von Huene, R., and D. Klaeschen (1999), Opposing gradients of permanent strain in the aseismic zone and elastic strain across the seismogenic zone of the Kodiak shelf and slope, Alaska, *Tectonics*, *18*(2), 248–262, doi:10.1029/1998TC900022.

von Huene, R., and C. R. Ranero (2003), Subduction erosion and basal friction along the sediment-starved convergent margin off Antofagasta, Chile, *J. Geophys. Res.*, *108*(B2), 2079, doi:10.1029/2001JB001569.

von Huene, R., and D. W. Scholl (1991), Observations at convergent margins concerning sediment subduction, erosion, and the growth of continental crust, *Rev. Geophys.*, *29*, 279–316, doi:10.1029/91RG00969.

von Huene, R., N. Nasu, and Y. Aoki (1986), The Japan Trench: Line ORI 78–4, in *Seismic Images of Modern Convergent Margins Tectonic Structure*, edited by R. von Huene, *AAPG Stud. Geol.*, *26*, 57–60.

von Huene, R., D. Klaeschen, B. Cropp, and J. Miller (1994), Tectonic structure across the accretionary and erosional parts of the Japan Trench margin, *J. Geophys. Res.*, *99*(B11), 22,349–22,361, doi:10.1029/94JB01198.

von Huene, R., C. R. Ranero, and P. Vannucchi (2004), Generic model of subduction erosion, *Geology*, *32*(10), 913–916, doi:10.1130/G20563.1.

Wang, K., and J. He (1999), Mechanics of low-stress forearcs: Nankai and Cascadia, *J. Geophys. Res.*, *104*(B7), 15,191–15,205, doi:10.1029/1999JB900103.

Wang, K., and J. He (2008), Effects of frictional behavior and geometry of subduction fault on coseismic seafloor deformation, *Bull. Seismol. Soc. Am.*, *98*(2), 571–579, doi:10.1785/0120070097.

Wang, K., and Y. Hu (2006), Accretionary prisms in subduction earthquake cycles: The theory of dynamic Coulomb wedge, *J. Geophys. Res.*, *111*, B06410, doi:10.1029/2005JB004094.

Wang, K., J. He, and Y. Hu (2006), A note on pore fluid pressure ratios in the Coulomb wedge theory, *Geophys. Res. Lett.*, *33*, L19310, doi:10.1029/2006GL027233.

Ye, S., J. Bialas, E. R. Flueh, A. Stavenhagen, R. von Huene, G. Leandro, and K. Hinz (1996), Crustal structure of the Middle American Trench off Costa Rica from wide-angle seismic data, *Tectonics*, *15*(5), 1006–1021, doi:10.1029/96TC00827.

Y. Hu, School of Earth and Ocean Sciences, University of Victoria, Petch Building 168, 3800 Finnerty Road, Victoria, BC V8P 5C2, Canada. (yanhu@uvic.ca)

K. Wang, Pacific Geoscience Centre, Geological Survey of Canada, 9860 West Saanich Road, P.O. Box 6000, Sidney, BC V8L 4B2, Canada.